Journal of Magnetic Resonance 209 (2011) 53–60

Contents lists available at ScienceDirect

Journal of Magnetic Resonance

journal homepage: www.elsevier.com/locate/jmr

Off-resonance saturation MRI of superparamagnetic nanoprobes: Theoretical models and experimental validations

Chalermchai Khemtong [a], Osamu Togao [b], Jimin Ren [b], Chase W. Kessinger [a], Masaya Takahashi [b], A. Dean Sherry [b], Jinming Gao [a,*]

[a] Department of Pharmacology, Harold C. Simmons Comprehensive Cancer Center, University of Texas Southwestern Medical Center, 5323 Harry Hines Boulevard, Dallas, TX 75390, United States
[b] The Advanced Imaging Research Center, University of Texas Southwestern Medical Center, 5323 Harry Hines Boulevard, Dallas, TX 75390, United States

ARTICLE INFO

Article history:
Received 13 September 2010
Revised 30 November 2010
Available online 5 January 2011

Keywords:
Magnetic resonance imaging
Transverse relaxivity
Off-resonance saturation
Superparamagnetic polymeric micelles
PEG corona length
Nanoprobes

ABSTRACT

Off-resonance saturation (ORS) is a new magnetic resonance imaging (MRI) method that has shown greatly improved contrast sensitivity for the detection of cancer-specific biomarkers by superparamagnetic nanoprobes *in vivo*. However, quantitative understanding of the ORS contrast mechanism and its dependence on the structural parameters of superparamagnetic nanoprobes are still lacking. Here we propose a quantitative model of ORS contrast and its experimental validation by superparamagnetic polymeric micelles (SPPM) with precisely controlled structural properties. Size selected, monodisperse Fe_3O_4 nanoparticles (6.1 ± 0.2 nm) were used to form a series of SPPM nanoprobes with specifically controlled corona thickness using 1,2-distearoyl-*sn*-glycero-3-phosphoethanolamine-*N*-methoxypoly(ethylene glycol) (DSPE-PEG) with different PEG molecular weights. Transmission electron microscopy and dynamic light scattering showed that SPPM were uniform in size. The average hydrodynamic diameters of SPPM with PEG lengths of 0.55, 1, 2, and 5 kD were 16.6 ± 2.8, 18.4 ± 2.9, 24.1 ± 3.4, and 28.9 ± 3.4 nm, respectively. MRI experiments at 7T determined that r_2 values of SPPM with 0.55, 1, 2, and 5 kD PEG as corona were 201 ± 3, 136 ± 8, 107 ± 5, and 108 ± 8 Fe mM^{-1} s^{-1}, respectively. ORS intensity from *Z*-spectra of SPPM showed a significant correlation with the inverse of T_2 relaxation rates ($1/T_2$, s^{-1}) of the SPPM nanoprobes regardless of the PEG corona thickness. These data provide the fundamental understanding of the structure–property relationships between the SPPM nanostructures and ORS sensitivity, which offers useful mechanistic insights for the future improvement of SPPM nanoprobes in cancer molecular imaging applications.

1. Introduction

Recent development of novel MR probes and new imaging methods with improved imaging sensitivity and specificity have rapidly advanced the use of MRI in molecular and cellular imaging applications [1–4]. Compared to the low molecular weight, paramagnetic metal chelates such as Gd-DTPA, superparamagnetic nanoparticles (e.g., Fe_3O_4 [5–7], $MnFe_2O_4$ [8], FeCo [9] nanocrystals) have demonstrated substantially higher molar relaxivities and improved sensitivity for *in vivo* MR imaging. Surface functionalization of superparamagnetic iron oxide (SPIO) nanoparticles has provided multiple examples of targeted contrast agents that specifically recognize tumor markers such as the receptors of transferrin [10], folate [11], and Her-2/neu [12,13]. Once bound to a targeted marker or after internalization into a cell, SPIO probes can create substantial disturbances in the local magnetic field leading to a rapid dephasing of protons and loss of MR signal intensity. T_2- or T_2^*-weighted (T_2/T_2^*-w) MR imaging methods are most commonly used for SPIO imaging. T_2^*-w images obtained by gradient echo (GRE) imaging sequences often have low signal-to-noise ratios. T_2^*-w MR imaging is also highly sensitive to the magnetic susceptibility produced by the presence of SPIO-based agents producing signal voids larger than the actual sizes of accumulated SPIO agents. Finally, image voids from SPIO agents may be difficult to differentiate from other tissue voids (e.g., air sacs in the lung or abdominal cavity) or void-like signals caused by severe magnetic anisotropy that can occur at tissue interfaces.

Due to the above limitations, several recent studies reported new imaging techniques to generate "positive" MRI contrast from SPIO-based agents [14–21], which can potentially improve imaging accuracy of these agents. Seppenwoolde et al. reported a technique called White Marker to track paramagnetic markers stationed in a catheter inserted into a pig's abdominal aorta [14]. The positive contrast was achieved by dephasing of background signal while the signal near the markers was not affected due to the dipole field

* Corresponding author.
E-mail address: jinming.gao@utsouthwestern.edu (J. Gao).

1090-7807/$ - see front matter © 2011 Elsevier Inc. All rights reserved.
doi:10.1016/j.jmr.2010.12.013

generated by the markers. Cunnigham et al. reported the use of a similar method to obtain positive contrast from cells labeled with superparamagnetic nanoparticles [15]. In another work, SPIO-labeled stem cells in rat hearts were visualized using a sweep imaging with Fourier transformation (SWIFT) technique, in which nuclei were excited by a swept radiofrequency excitation with simultaneous signal acquisition [16]. Positive contrasts of SPIO-labeled stem cells were generated in the imaginary component, which can be registered with anatomical images of similar imaging planes. Recently, Zurkiya et al. and our research group have reported an off-resonance saturation (ORS) method to produce positive contrast of SPIO nanoparticles [19–21]. This technique involved the application of an RF pulse at an off-resonance frequency and the positive contrast was obtained by taking the ratio or subtraction of the images with and without the saturation.

Our previous study has demonstrated the effectiveness of ORS method for *in vivo* detection of tumor-targeted superparamagnetic polymeric micelles (SPPM) in tumor-bearing mice [21]. The ultrasensitive SPPM design provided a significant increase in sensitivity of detection by ORS MRI to the picomolar range of the nanoparticles. The ORS technique also improved the imaging accuracy compared to conventional T_2^*-weighted imaging method. This technique also allowed for visualization of image contrast without a pre-contrast acquisition. The ability to provide increased imaging sensitivity and accuracy while producing positive contrast has made ORS a promising technique for MR molecular imaging of SPPM. In this report, we describe the development of a theoretical model to quantitatively understand the ORS contrast mechanism, while experimentally validating the model using a set of structurally defined SPPM nanoprobes.

2. ORS theory

2.1. Fast diffusion and quantitative ORS model

When a SPPM particle is magnetized by an external magnetic field, the relaxation times of neighboring water protons are greatly shortened (Fig. 1). First, we assume that all outer-sphere (OS) water molecules diffuse rapidly on the NMR time scale and that the bulk water signal can be characterized by a single set of longitudinal (T_1) and transverse (T_2) relaxation times (Fig. 1a). After applying a soft continuous wave RF pulse at a power level of ω_1 ($\omega_1 = 2\pi B_1$, B_1 in Hz) and a frequency offset Ω for a duration of t, the magnetization of the attenuated water signal can be described by the Bloch equation:

$$\frac{dM(t)}{dt} = AM(t) + B \tag{1}$$

where $M(t) = \begin{bmatrix} Mx(t) \\ My(t) \\ Mz(t) \end{bmatrix}$, $A = \begin{bmatrix} \frac{1}{T_2} & \Omega & 0 \\ -\Omega & \frac{1}{T_2} & \omega_1 \\ 0 & -\omega_1 & \frac{1}{T_1} \end{bmatrix}$, $B = \begin{bmatrix} 0 \\ 0 \\ Mz^o/T_1 \end{bmatrix}$

and Mz^o is the equilibrium Z-magnetization component in the static external magnetic field.

The solution of Bloch equation can be expressed as

$$M(t) = M_\infty + e^{-At}(M^o - M^\infty) \tag{2}$$

where M^o is the magnetization vector at initial state prior to saturation, and M^∞ is the magnetization at steady-state,

$$M^\infty = \begin{bmatrix} Mx^\infty \\ My^\infty \\ Mz^\infty \end{bmatrix} = -A^{-1}B, \tag{3}$$

$$Mz^\infty = \frac{\left(1 + \Omega^2 T_2^2\right) Mz^o}{1 + \Omega^2 T_2^2 + \omega_1^2 T_1 T_2} \tag{4}$$

Note that the second term of Eq. (2) represents the magnetization difference between the initial and steady-state, modulated by a time-dependent function e^{-At} (e^{-At} converges to 0 at $t \to \infty$).

Eq. (4) is central to the understanding of the steady-state Z-magnetization (Mz^∞ and thereafter referred to as Mz) and its relationship with MRI parameters. The dependence of Z-magnetization on RF saturation power (ω_1), saturation frequency offset (Ω), and the relaxation times T_1 and T_2 can be predicted and quantified using this equation. Z-magnetization (Mz/Mz^o) [22] of a solution with given relaxation times, T_1 and T_2, is highly influenced by offset saturation frequency (Ω). At a saturation frequency far away from the bulk water peak, $|\Omega| \to \infty$, Mz/Mz^o is approximately 1 as the $\Omega^2 T_2^2$ term becomes the dominant factor in the equation. In other words, the ORS intensity is negligible because the initial and steady-state Z-magnetizations are equivalent. Conversely, a decrease in Mz/Mz^o or more pronounced ORS contrast is expected, when the saturation frequency offset is approaching the on-resonance frequency of water, or $|\Omega| \to 0$ ppm. The $\Omega^2 T_2^2$ term becomes less dominating and the relaxation times play a bigger role in dictating the ORS intensity resulting in smaller Mz/Mz^o.

2.2. Approximation of ORS models

In our previous work, we have shown ORS of SPPM solutions and its dependence on saturation frequency and SPPM concentration [21]. For *in vivo* ORS imaging, we used pre-determined imaging parameters such as saturation power ω_1 and frequency offset Ω. With these known parameters, it is possible to predict and quantify the ORS intensity (Mz/Mz^o). To test its feasibility, Eq. (4) is further derived to propose a simplified model to quantify the ORS intensity of SPPM.

Eq. (4) can be rearranged to

$$\frac{Mz}{Mz^o} = \frac{1}{1 + \omega_1^2 \frac{T_1 T_2}{1 + \Omega^2 T_2^2}} = \frac{1}{1 + x} \tag{5}$$

where $x = \omega_1^2 \frac{T_1 T_2}{1 + \Omega^2 T_2^2}$, which is further rearranged to: $x = \left(\frac{\omega_1}{\Omega}\right)^2 \frac{T_1 T_2}{\frac{1}{\Omega^2} + T_2^2}$

Under ORS conditions with a relatively large Ω (e.g. $\Omega \geqslant 900$ Hz or 3 ppm), where $1/\Omega^2 \ll T_2^2$, Eq. (5) becomes:

$$\frac{Mz}{Mz^o} = \frac{1}{1 + \left(\frac{\omega_1}{\Omega}\right)^2 \frac{T_1}{T_2}} \approx 1 - \left(\frac{\omega_1}{\Omega}\right)^2 \frac{T_1}{T_2} \tag{6}$$

Eq. (6) shows a linear relationship between the ORS intensity and longitudinal relaxation time (T_1) and inverse of transverse relaxation time ($1/T_2$) of SPPM solutions at a given saturation power and frequency. In tissue samples, Eq. (6) can be further derived to show the correlation between the ORS intensity and SPPM concentration.

$$\frac{Mz}{Mz^o} = 1 - T_1 \left(\frac{\omega_1}{\Omega}\right)^2 \left(\frac{1}{T_2 \text{endo}} + r_2[SPPM]\right) \tag{7}$$

where $\frac{1}{T_2} = \left(\frac{1}{T_2 \text{endo}} + r_2[SPPM]\right)$, and T_2endo = endogenous T_2 relaxation time.

Because T_2endo is longer than 200 ms and SPPM probes have high r_2 values, then $1/T_2\text{endo} \ll r_2[\text{SPPM}]$. Eq. (7) subsequently becomes:

$$\frac{Mz}{Mz^o} = 1 - T_1 \left(\frac{\omega_1}{\Omega}\right)^2 (r_2[SPPM]) \tag{8}$$

A linear relationship between ORS intensity and SPPM concentration is depicted in Eq. (8). This equations shows that ORS intensity of strongly dependent on T_2 relaxivity and concentration of SPPM probes in addition to its dependence on saturation power and offset frequency. It is important to note, however, that similar substitution of $(1/T_1\text{endo} + r_1[\text{SPPM}])$ for $1/T_1$ will not simplify the

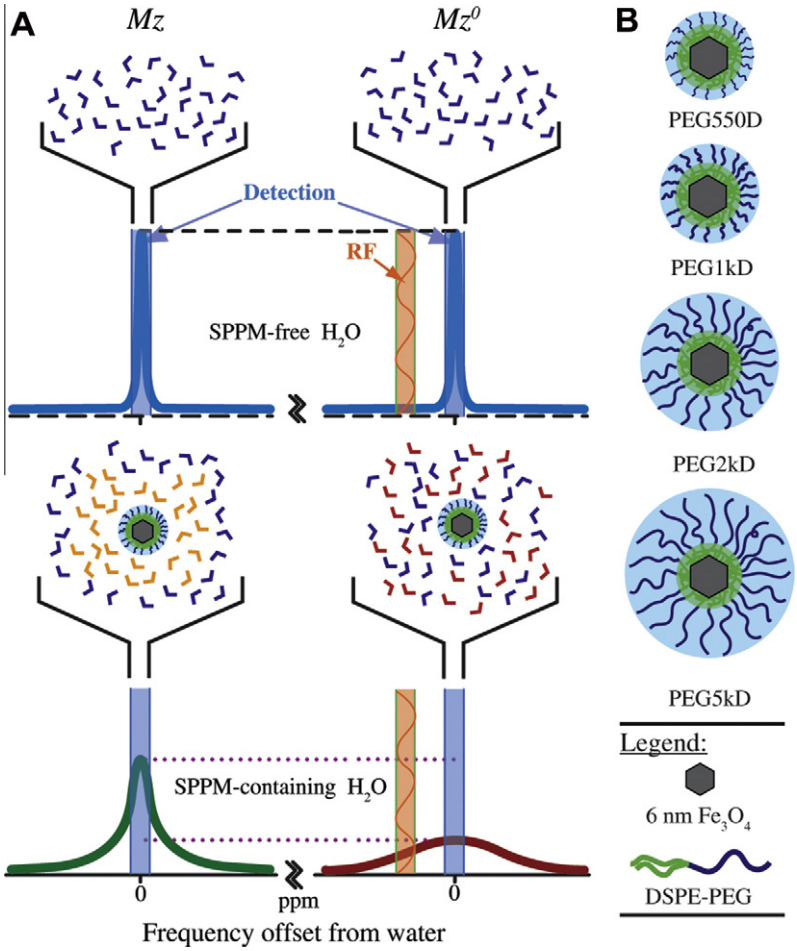

Fig. 1. (A) Illustration of mechanism of SPPM-induced ORS contrast, and (B) a schematic representation of SPPM with different PEG corona lengths but the same Fe_3O_4 core. In ORS contrast, an off-resonance RF saturation pulse only affects the SPPM-containing water protons. Due to fast water diffusion and long RF duration time, a steady-state is reached with lower signal intensity.

equation because both terms will likely be in the same order of magnitude. This is because SPPM formulations are not effective T_1 relaxation agents with low r_1 values.

3. Experimental section

3.1. Preparation of SPPM

Fe_3O_4 nanoparticles (or SPIO) were synthesized from iron(III) acetylacetonate in benzyl ether based on a published procedure [23]. After synthesis, the particles were size-selected by repeated precipitation with ethanol from hexane to yield monodisperse Fe_3O_4 nanoparticles (6.1 ± 0.2 nm) as confirmed by transmission electron microscopy (TEM). 1,2-Distearoyl-*sn*-glycero-3-phosphoethanolamine-*N*-methoxypoly(ethylene glycol) (DSPE-PEG) with PEG molecular weights of 0.55, 1, 2, 5 kD (Avanti Polar Lipids, Inc. Alabaster, Alabama) were used to produce SPPM following a published procedure with slight modification [24]. Briefly, a mixture of SPIO (100 μg) and DSPE-PEG (2.5 mg) in THF was dried with a flow of argon generating a thin film. The film was rehydrated with pH 7.4 HEPES (10 mM) buffer that contains 150 mM NaCl (1 mL) at 70 °C. The mixture was vortexed for 5 min and incubated at 70 °C for 3 h with intermittent vortexing. The resulting mixture was then diluted with deionized water (3 mL), filtered through a nylon filter membrane (size cutoff 0.2 μm), and then concentrated using an Amicon Centrifugal Filter. SPPMs were collected and the final volume was adjusted to 1 mL.

3.2. Characterization of SPPM

All formulations of SPPM were characterized by TEM and dynamic light scattering (DLS). Carbon-coated TEM grids were subject to a glow-discharge treatment using a plasma etcher. A drop of a SPPM solution was placed on the hydrophilic grid for 2 min. After the SPPM solution was removed, a solution of 2% phosphotungstic acid (PTA, pH = 7.4) was placed on the grid for 30 s. The grids containing SPPM samples were then analyzed on a JOEL 1200 EX TEM microscope at an accelerating voltage of 120 kV. For size distribution analysis, SPPM solutions were centrifuged at 5000 rpm for 1 min before subjecting to size measurements using a Viscotek 802 DLS instrument (Houston, TX) equipped with a He-Ne laser (λ = 825 nm). Scattered light was collected at 90° and data were analyzed from 50 measurements at 20 °C. Iron concentration of SPPM solutions were measured by atomic absorption spectroscopy (AAS). First, a known volume of SPPM solutions were digested in aqua regia at 70 °C for 3 h. The solution was then diluted and the actual iron contents were determined using a Varian SpectrAA 50 (Varian Inc., Palo Alto, CA) spectrometer. The calibration curve was obtained using an iron standard solution (Sigma Aldrich, St. Louis, MO).

3.3. Magnetic resonance imaging

All MR experiments were performed on a 7T small animal imager with a 40 mm i.d. Millipede coil (Varian, Inc, Palo Alto, CA). The SPPM sample was placed in a 1 mL plastic syringe with both ends sealed with paraffin wrap. The syringes contained SPPM solutions with different concentrations (50, 100, 250, 500, 1000 μM Fe) and were inserted into a 10 mL plastic syringe, which was filled with deionized water and sealed with paraffin. T_1 measurements were carried out using an inversion recovery pulse sequence with TR = 15 s, TE = 2.13 ms, and flip angle = 6°. Inversion time (TI) was arrayed from 5.1 ms to 10 s. The null intensity point of the series of TI-varying MRI images for each solution was visually verified and was used to cross-check the T_1 values obtained from data fitting the curves of MRI intensity versus TI. T_2 times of SPPM solutions were measured using a fast spin echo pulse sequence with TR = 2 s and TE = 7, 15, 20, 30, 45, 60, 90, 150, 300, 500 ms. ORS experiments were carried out using a spin echo (SE) pulse sequence (TR = 2 s, TE = 8.5 ms), with a pre-saturation B_1 power of 1.75 μT for 0.5 s. The off-resonance saturation frequencies (Ω) were 15, ±3, ±1.5, ±1.2, ±0.9, ±0.6, ±0.3, or 0 kHz from bulk water. The image obtained with the saturation frequency of 15 kHz (or 50 ppm) was used as a reference image. All experiments were conducted in triplicate using three different SPPM sample preparation for each formulation.

3.4. Data analysis

The MR images were analyzed using ImageJ (NIH). The relaxivity values (i.e. r_1 and r_2) were calculated using a least-squares curve fitting of the reciprocal of relaxation times (i.e. $1/T_1$ and $1/T_2$) versus iron concentrations ([Fe]). For ORS experiments, the Mz/Mz^o division images were generated by pixel-by-pixel division of the saturation image by the reference image. The *Z*-spectra were generated by plotting Mz/Mz^o versus saturation frequencies from the bulk water peak. Comparison of apparent Mz/Mz^o values obtained from MRI experiments with theoretical calculations based on Eq. (4) was achieved using MATLAB (MathWorks, Natick, MA).

4. Results and discussion

A set of single SPIO-loaded micelles encapsulated by PEGylated phospholipids was used in this study (Fig. 1b). A monodisperse distribution of SPIO nanoparticles (Fig. 2a) was employed to ensure the uniformity of the resulting micelle samples. PEG corona thickness was controlled by the use of DSPE-PEG lipids with varying PEG molecular weights from 0.55 to 5 kD. Each SPPM contained only one SPIO nanoparticle due to the short hydrophobic distearoyl chains of the phospolipid. TEM analyses revealed that all of the SPPM samples had a core–shell structure (Fig. 2), where staining with 2% PTA solution showed bright circles of the SPPM's hydrophobic cores encasing black SPIO nanoparticles. SPPMs are highly uniform with comparable core sizes (~13 nm) across all formulations (Fig. 2d–f). This is consistent with expected results due to each formulation containing the same disteraoyl lipid segment for SPIO encapsulation. DLS analysis showed the hydrodynamic diameters of SPPM became larger with an increase in PEG lengths. More specifically, the average diameters were 16.6 ± 2.8, 18.4 ± 2.9, 24.1 ± 3.4, and 28.9 ± 3.4 nm for the SPPM with PEG corona lengths of 0.55, 1, 2, 5 kD, respectively. The data confirmed that higher molecular weight of PEG will result in larger hydrated layer and thus larger hydrodynamic diameter of SPPM. The difference in hydrodynamic diameter between each SPPM formulation as a result of differing PEG molecular weights agrees well with an estimation of micelles' corona length based on PEG's molecular weight and radius of gyration [25]. This series of SPPM, with well-controlled structures, provided an excellent experimental system for the validation of the proposed ORS theory.

MR relaxivities of all SPPM formulations were first investigated. T_1 and T_2 relaxation times of SPPM solutions were measured with Fe concentrations ranging from 50 μM to 1 mM. T_1 and T_2 relaxivity values (r_1 and r_2) are summarized in Fig. 3. T_2 relaxivity decreased with an increase of the PEG molecular weight despite all the SPPM formulations containing the same SPIO core. Average r_2 values ($n = 3$) were 201 ± 3, 136 ± 8, 107 ± 5, and 108 ± 8 s^{-1} mM^{-1} Fe for SPPMs with 0.55, 1, 2, 5 kD PEG as corona, respectively. These results are consistent with those from LaConte et al., in which a similar trend was observed in the study of an effect of PEG length on T_2 relaxation rate ($1/T_2$) of monocrystalline iron oxide (MION) nanoparticles [26]. In contrast to transverse relaxation, the PEG length did not significantly affect the longitudinal relaxation of SPPM where r_1 values are statistically equivalent (0.7–0.8 s^{-1} mM^{-1} Fe) from different formulations (Fig. 3).

Next, we measured the dependence of ORS intensity on the off-resonance saturation frequency (Ω) at different SPPM concentrations. The Ω values were varied from 0 to 10 ppm on both positive and negative sides of the bulk water resonance frequency. Fig. 4 shows a representative ORS image analysis of a SPPM sample with 5 kD PEG. SPPM-induced image darkening was visible (Fig. 4a) when the saturation frequency was closer to the water peak ($|\Omega| \rightarrow 0$ ppm). The fire-color-coded images are ORS images obtained by taking a division of spin-echo images with and without saturation (Mz/Mz^o). Fig. 4b plotted the ORS intensity as a function of Ω at four different SPPM concentrations. It is important to note that experimental data (red[1] squares in Fig. 4b) and theoretical calculations (blue curves) provide a close fit for all four different SPPM concentrations. The theoretical data were calculated using Eq. (4) and other pre-determined parameters (e.g. T_1 and T_2 of each SPPM solution and pre-saturation (B_1) power: $\omega_1 = 1.75$ μT or 75 Hz). These data validate the quantitative ORS models as derived from Bloch equations based on the steady-state assumption under the current pre-saturation conditions ($\omega_1 = 1.75$ μT, $t = 500$ ms). These results complement the ORS model by Hu and Zurkiya [19], where the authors elegantly demonstrated that water diffusion instead of water exchange-mediated magnetization transfer as the primary causation of ORS contrast. In their model, the retention time of water molecules in magnetic isosurfaces approximated by the dipole field is a key factor in generating the ORS contrast. Therefore, the diffusion rate of water molecules is an important driving force of the ORS contrast generating mechanism. It should be noted that a gradient echo sequence with short pre-saturation pulse (6 ms Gaussian pulse) was used in the reported study, which may not permit the steady-state assumption as allowed in our study (see *Supplementary* Fig. S1 for the reaching of steady-state at different B_1 power and saturation durations). Future work is necessary to examine the specific ORS acquisition conditions and boundary conditions that would allow for the quantitative correlation with MR relaxation parameters of the superparamagnetic nanoprobes.

Under our current model, the complete quantitative ORS expression (Eq. (4)) can be greatly simplified at a relatively large Ω (e.g. $\Omega \geqslant 900$ Hz or 3 ppm). Under this condition, the ORS intensity (Mz/Mz^o) becomes linearly correlated with T_1/T_2 (Eq. (6)). First, we plotted the ORS intensity as a function of iron concentration for different SPPM nanoprobes. The left panel of Fig. 5 shows that SPPM with the shortest PEG corona (i.e. 0.55 kD) demonstrated the highest concentration-dependent ORS intensity over SPPM with longer PEG corona. The ORS sensitivity (slope) increased with

[1] For interpretation of color in Figs. 1–5, the reader is referred to the web version of this article.

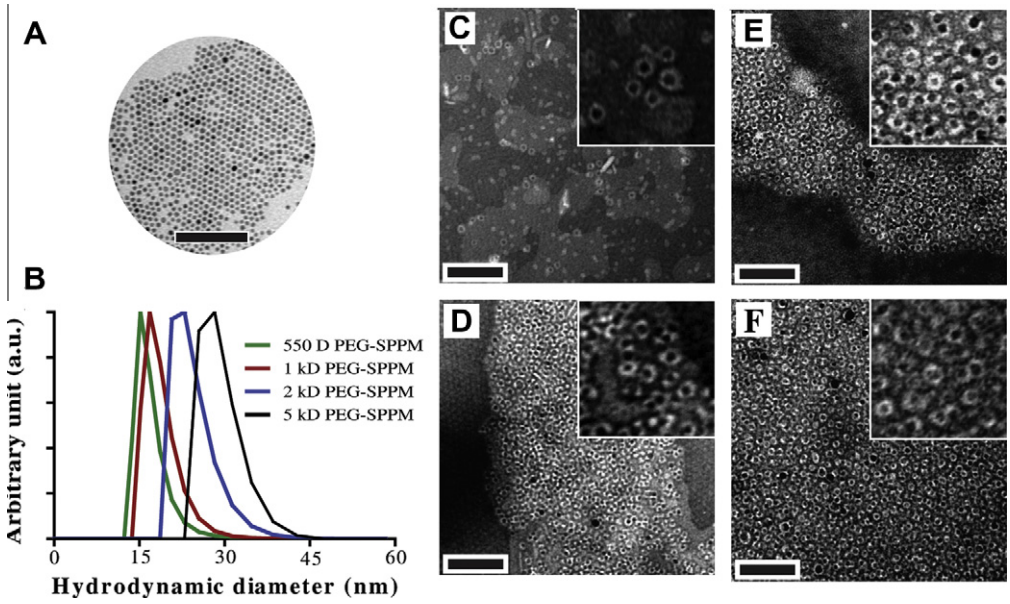

Fig. 2. (A) TEM of as-synthesized Fe_3O_4 (6.1 ± 0.2 nm), (B) size distribution of SPPM by DLS, (C–F) TEM of SPPM with PEG molecular weights of 550 D, 1 kD, 2 kD, or 5 kD after staining with 2% PTA solution, respectively. The insets show the amplified images of a few particles. All scale bars are 100 nm.

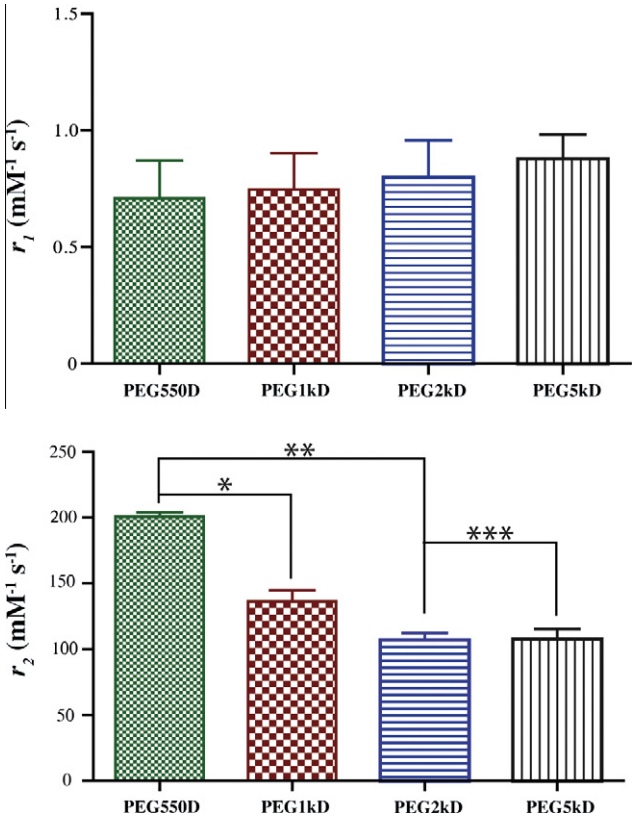

Fig. 3. T_1 (top) and T_2 (bottom) relaxivities (r_1 and r_2) of SPPM with different PEG corona lengths. The difference in r_1 values across all formulations is not statistically significant. The single and double asterisks (* and **) indicate statistical significance ($P < 0.05$) between the SPPM groups of interest. r_2 values of SPPM with 2 kD and 5 kD PEG are statistically equivalent (***, $P > 0.05$).

decrease of PEG lengths, i.e., PEG 0.55 kD > PEG 1 kD > PEG 2 kD ≈ PEG 5 kD. Similar to the T_2 relaxivity study, SPPM samples with a PEG corona of 2 or 5 kD showed an almost identical ORS dependence on [Fe]. This trend is well supported by Eq. (8) showing the relationship between ORS intensity and transverse relaxivity values of SPPM nanoprobes. Interestingly, when the ORS intensity was plotted as a function of T_2 relaxation rates (right panel, Fig. 5), all the data points from different SPPM samples collapsed into a single linear correlation. Such linear relationship can be explained by the low longitudinal relaxivity of all SPPM formulations, which will result in comparable T_1 times due to the small r_1 values (0.7–0.9 Fe mM^{-1} s^{-1} with a standard deviation of approximately 0.1 Fe mM^{-1} s^{-1}). This result also suggests that the difference in T_1 relaxivites between SPPM formulations will be small relative to endogenous T_1 times in samples or tissues resulting in equivalent T_1 times for all samples. Since saturation power (ω_1) and frequency (Ω) are pre-determined parameters, the $T_1(\omega_1/\Omega)^2$ term becomes a constant. The resulting ORS intensity is then linearly correlated with T_2 relaxation rate as predicted by Eq. (6). These data suggest that for SPPM nanoprobes, T_2 relaxation rate is a predominant factor that directly affects the ORS sensitivity of detection.

Our previous report has demonstrated the effectiveness of the ORS method to image αvβ3 integrins on tumor vasculature in a tumor-bearing animal by cRGD-encoded SPPM nanoprobes [21] Compared to conventional T_2/T_2^*-weighted imaging, the ORS method does not require pre-contrast scanning and, moreover, the contrast sensitivity can be greatly enhanced by the direct comparison between the "ON" and "OFF" images (i.e. with and without the presaturation) for SPIO-specific contrast. Despite these advantages, ORS imaging, like many other MRI techniques, can still benefit from a highly sensitive design of contrast probes for improved detection. Results from this study established the quantitative correlation of ORS intensity with the imaging acquisition conditions and microscopic structures and MR relaxation properties of the nanoprobes. This knowledge has several valuable implications for the optimized design of MR nanoprobes. First, ORS intensity is directly correlated to T_1 and T_2 of the nanoprobe and, in a simplified model (Eq. (6)), is proportional to the ratio of T_1/T_2. This suggests that an ideal ORS contrast probe should be a "pure" T_2 agent with minimal capability for T_1 relaxation. Simulations of ORS intensity (Mz/Mz^o) using Eq. (4) clearly show that the ORS effect is larger (Mz/Mz^o is smaller) when T_1 is longer (*Fig.* S1). However, longer T_1 values also require a longer pre-saturation period to reach

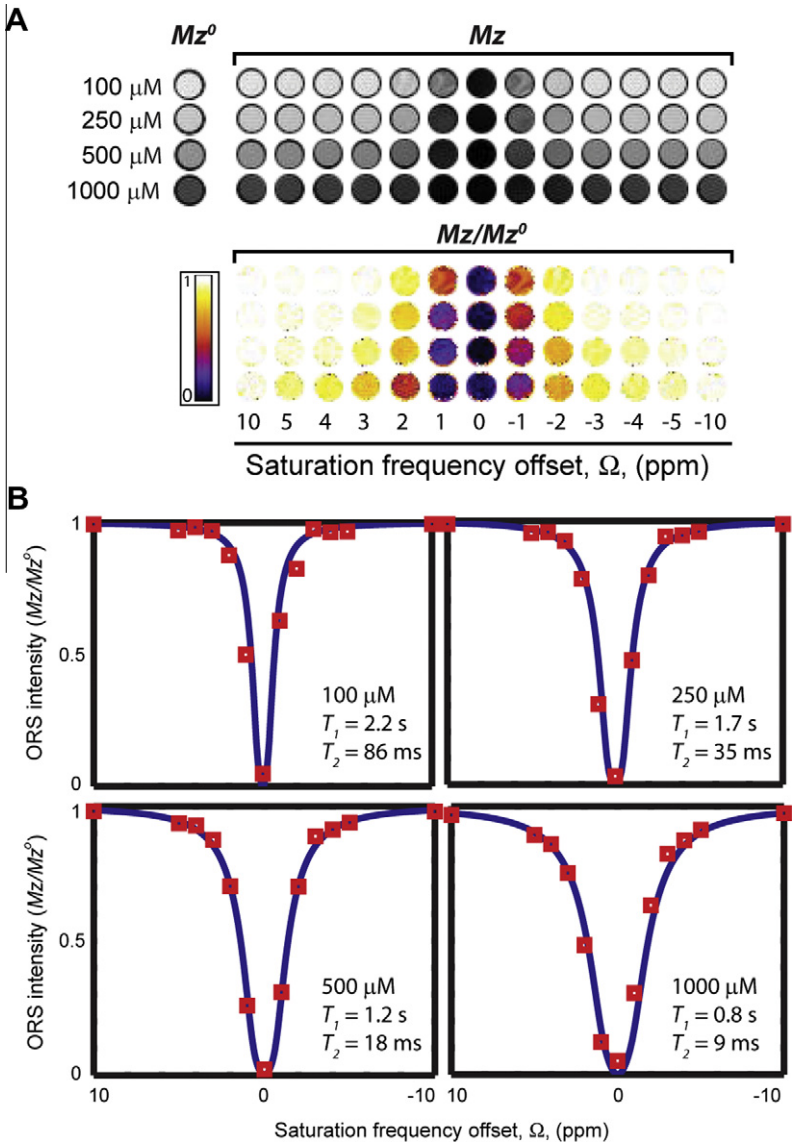

Fig. 4. ORS analysis of SPPM at different saturation frequency offsets. (A) Proton density images of SPPM at different concentrations obtained with RF saturation frequencies (top) and their corresponding division images (Mz/Mz^o, bottom). (B) Simulated and experimental Z-spectra of corresponding SPPM. Experimental data are shown as red squares and the curves were calculated using Eq. (4) and actual T_1 and T_2 values of the SPPM sample. The corona length of SPPM is 5 kD (5 kD PEG). SPPM concentrations were shown as μM Fe. Imaging parameters: TR = 2 s, TE = 8.5 ms, saturation power (ω_1) = 1.75 μT, saturation duration = 500 ms, off-resonance saturation frequency (Ω) = varied. (For interpretation of the references to colour in this figure legend, the reader is referred to the web version of this article.)

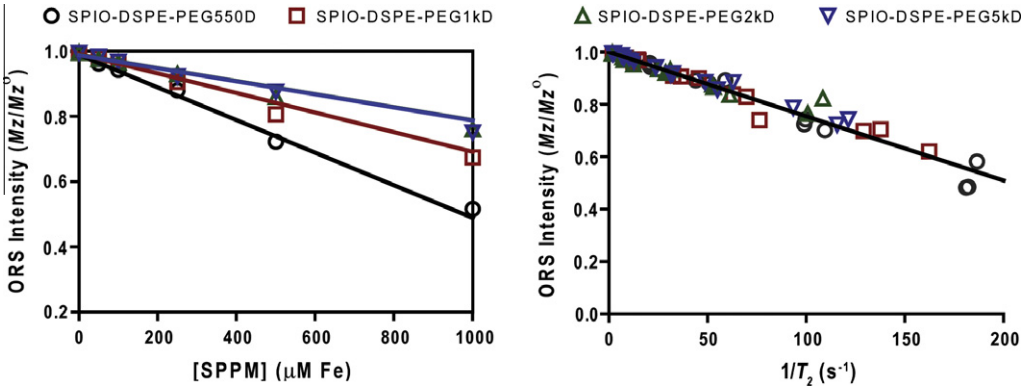

Fig. 5. ORS intensity as a function of Fe concentration (left) and T_2 relaxation rates (right) for SPPMs with different PEG corona thickness. Imaging parameters: TR = 2 s, TE = 8.5 ms, saturation power (ω_1) = 1.75 μT, saturation duration = 500 ms, off-resonance saturation frequency (Ω) = 3 ppm.

steady-state. The current SPPM design, where the as-synthesized SPIO is coated with hydrophobic oleic acids and further encapsulated in the hydrophobic core of the micelles, can effectively minimize direct contact with water molecules and result in significantly reduced T_1 relaxivity as demonstrated by the experimental data (r_1 = 0.7–0.9 Fe mM^{-1} s^{-1}, Fig. 3a) [27]. In comparison, the hydrophilic SPIO nanoparticles (e.g. by base precipitation method in dextran matrix) had higher T_1 relaxivity (e.g. r_1 = 23.9 Fe mM^{-1} s^{-1} for Feridex) [28]. Consequently, results from Feridex and Gd-doped Feridex solutions show reduced ORS sensitivity (see *Fig.* S1) as a result of shorter T_2 time and longer T_1 time of Feridex compared to those of SPPM. On the other hand, strategies to increase the T_2 relaxivity of the contrast agents will also lead to enhanced ORS detection. Development of highly magnetized superparamagnetic nanoparticles (e.g. FeCo [9], $MnFeO_4$ [8], Zn-SPIO [29]) or SPIO-clustered micelles [30] will considerably increase the sensitivity of ORS detection. Second, although results from this study show that SPPM with shorter PEG length (e.g. 0.55 kD) have higher ORS sensitivity, it may not have sufficient stability in blood. For example, a 2 kD PEG length was used in the liposomal delivery of doxorubicin, which has demonstrated prolonged circulation and blood half-life of the nanoparticles [31]. Consequently, an optimal PEG length needs to be investigated to provide the best compromise between ORS sensitivity and desirable pharmacokinetics. Third, use of higher B_1 power (ω_1) and smaller frequency offset (Ω) can also further increase ORS sensitivity (Eqs. (4), (6), and (8)). However, increase of B_1 power should be carefully examined to stay below the limit of maximum specific absorption rate (i.e. 4 W/kg body weight) for RF exposure [32,33], in particular for future clinical applications. Finally, higher magnetic fields are also beneficial to ORS imaging as shorter T_2 times and longer T_1 times of MRI contrast agents at higher fields [34] contribute to higher ORS contrast enhancement as suggested in Eqs. (6) and (8).

The combination of the ORS method and the ultrasensitive SPPM design is a great asset for MR molecular imaging applications, in which improved sensitivity and detection accuracy are highly desirable. Much work still needs to be performed in order for clinical translation of this technique. One shortcoming for current exogenous imaging agents such as SPIO-based probes and PARACEST complexes [35] is their limited targeting specificity to the disease locations. However, a number of strategies using cell-specific ligands have been reported to improve the accumulations of these agents at targeted sites such as tumorous tissues [8,21] and atherosclerotic plaques [36,37]. Our SPPM design offers greatly improved MR sensitivity as evidenced by their high relaxivity values [30]. ORS imaging allows for additional benefits in accurate detection of SPPM. This combination may offer considerable advantages over other class of MR agents with limited detection sensitivity and contribute to the existing arsenals of imaging tools for molecular diagnosis of cancer and other diseases.

5. Conclusions

In summary, we have established the theoretical framework and quantitative expressions to describe the ORS contrast mechanism of SPPM nanoprobes. The proposed ORS theory was well supported by the experimental data from a series of precisely controlled SPPMs with varied PEG lengths. Results showed that the thickness of PEG corona is a critical parameter that greatly affected MR relaxivity and ORS sensitivity of SPPM. The proposed ORS theory was able to quantitatively predict the contrast enhancement of a given SPPM solution with known relaxation times T_1 and T_2. Results from this study provide the mechanistic insights on the ORS contrast sensitivity of SPPM nanoparticles, which will assist the future development of SPPM as ultrasensitive MRI nanoprobes for *in vivo* imaging applications.

Disclosure statement

None declared.

Acknowledgment

We thank the financial support from the following agencies: National Institutes of Health (R21 EB005394 and R01 CA129011 to JG, NIH CA15531 to ADS) and Robert A. Welch Foundation (AT-584 to ADS). C. Khemtong was supported by a Department of Defense Breast Cancer Research Program Multidisciplinary Postdoctoral Award (W81XWH-06-1-0751).

Appendix A. Supplementary material

Supplementary data associated with this article can be found, in the online version, at doi:10.1016/j.jmr.2010.12.013.

References

[1] Y.W. Jun, J.H. Lee, J. Cheon, Chemical design of nanoparticle probes for high-performance magnetic resonance imaging, Angew. Chem. Int. Ed. 47 (2008) 5122–5135.
[2] C. Khemtong, C.W. Kessinger, J.M. Gao, Polymeric nanomedicine for cancer MR imaging and drug delivery, Chem. Commun. 24 (2009) 3497–3510.
[3] H.B. Na, I.C. Song, T. Hyeon, Inorganic nanoparticles for MRI contrast agents, Adv. Mater. 21 (2009) 2133–2148.
[4] R. Weissleder, M.J. Pittet, Imaging in the era of molecular oncology, Nature 452 (2008) 580–589.
[5] J.W. Bulte, D.L. Kraitchman, Iron oxide MR contrast agents for molecular and cellular imaging, NMR Biomed. 17 (2004) 484–499.
[6] D.L. Thorek et al., Superparamagnetic iron oxide nanoparticle probes for molecular imaging, Ann. Biomed. Eng. 34 (2006) 23–38.
[7] Y.X.J. Wang, S.M. Hussain, G.P. Krestin, Superparamagnetic iron oxide contrast agents: physicochemical characteristics and applications in MR imaging, Eur. Radiol. 11 (2001) 2319–2331.
[8] J.H. Lee et al., Artificially engineered magnetic nanoparticles for ultra-sensitive molecular imaging, Nat. Med. 13 (2007) 95–99.
[9] W.S. Seo et al., FeCo/graphitic-shell nanocrystals as advanced magnetic-resonance-imaging and near-infrared agents, Nat. Mater. 5 (2006) 971–976.
[10] D. Hogemann-Savellano et al., The transferrin receptor: a potential molecular imaging marker for human cancer, Neoplasia 5 (2003) 495–506.
[11] F. Sonvico et al., Folate-conjugated iron oxide nanoparticles for solid tumor targeting as potential specific magnetic hyperthermia mediators: synthesis, physicochemical characterization, and in vitro experiments, Bioconjug. Chem. 16 (2005) 1181–1188.
[12] D. Artemov et al., MR molecular imaging of the Her-2/neu receptor in breast cancer cells using targeted iron oxide nanoparticles, Magn. Reson. Med. 49 (2003) 403–408.
[13] M.A. Funovics et al., MR imaging of the her2/neu and 9.2.27 tumor antigens using immunospecific contrast agents, Magn. Reson. Imag. 22 (2004) 843–850.
[14] J.H. Seppenwoolde, M.A. Viergever, C.J. Bakker, Passive tracking exploiting local signal conservation: the white marker phenomenon, Magn. Reson. Med. (2003) 784–790.
[15] C.H. Cunningham et al., Positive contrast magnetic resonance imaging of cells labeled with magnetic nanoparticles, Magn. Reson. Med. 53 (2005) 999–1005.
[16] R. Zhou et al., SWIFT detection of SPIO-labeled stem cells grafted in the myocardium, Magn. Reson. Med. 63 (2010) 1154–1161.
[17] A.A. Gilad et al., MR tracking of transplanted cells with "positive contrast" using manganese oxide nanoparticles, Magn. Reson. Med. 60 (2008) 1–7.
[18] V. Mani et al., Gradient echo acquisition for superparamagnetic particles with positive contrast (GRASP): sequence characterization in membrane and glass superparamagnetic iron oxide phantoms at 1.5 T and 3 T, Magn. Reson. Med. 55 (2006) 126–135.
[19] O. Zurkiya, X. Hu, Off-resonance saturation as a means of generating contrast with superparamagnetic nanoparticles, Magn. Reson. Med. 56 (2006) 726–732.
[20] J. Ren, et al., SPIO MRI contrast can be enhanced by off-resonance saturation, in: The Fifth Annual Meeting of the Society for Molecular Imaging, Waikoloa, Hawaii, USA, 2006.
[21] C. Khemtong et al., In vivo off-resonance saturation magnetic resonance imaging of alpha(v)beta(3)-targeted superparamagnetic nanoparticles, Cancer Res. 69 (2009) 1651–1658.
[22] J. Grad, R.G. Bryant, Nuclear magnetic cross-relaxation spectroscopy, J. Magn. Reson. 90 (1990) 1–8.
[23] S.H. Sun et al., Monodisperse MFe_2O_4 (M = Fe, Co, Mn) nanoparticles, J. Am. Chem. Soc. 126 (2004) 273–279.

[24] B. Dubertret et al., In vivo imaging of quantum dots encapsulated in phospholipid micelles, Science 298 (2002) 1759–1762.
[25] D. Sutton et al., Doxorubicin and beta-lapachone release and interaction with micellar core materials: experiment and modeling, Exp. Biol. Med. 232 (2007) 1090–1099.
[26] L.E.W. LaConte et al., Coating thickness of magnetic iron oxide nanoparticles affects R-2 relaxivity, J. Magn. Reson. Imag. 26 (2007) 1634–1641.
[27] H.W. Duan et al., Reexamining the effects of particle size and surface chemistry on the magnetic properties of iron oxide nanocrystals: new insights into spin disorder and proton relaxivity, J. Phys. Chem. C 112 (2008) 8127–8131.
[28] R. Weissleder et al., Superparamagnetic iron oxide: pharmacokinetics and toxicity, AJR Am. J. Roentgenol. 152 (1989) 167–173.
[29] C. Barcena et al., Zinc ferrite nanoparticles as MRI contrast agents, Chem. Commun. 19 (2008) 2224–2226.
[30] H. Ai et al., Magnetite-loaded polymeric micelles as ultrasensitive magnetic-resonance probes, Adv. Mater. 17 (2005) 1949–1952.
[31] D. Sutton et al., Functionalized micellar systems for cancer targeted drug delivery, Pharmaceut. Res. 24 (2007) 1029–1046.
[32] P.A. Bottomley et al., Estimating radiofrequency power deposition in body NMR imaging, Magn. Reson. Med. 2 (1985) 336–349.
[33] D.I. Hoult, C.N. Chen, V.J. Sank, The field dependence of NMR imaging. II. Arguments concerning an optimal field strength, Magn. Reson. Med. 3 (1986) 730–746.
[34] H. Uematsu et al., A direct comparison of signal behavior between 4.0 and 1.5 T: a phantom study, Eur. J. Radiol. 45 (2003) 154–159.
[35] S. Viswanathan et al., Alternatives to gadolinium-based metal chelates for magnetic resonance imaging, Chem. Rev. 110 (2010) 2960–3018.
[36] M.J. Lipinski et al., MRI to detect atherosclerosis with gadolinium-containing immunomicelles targeting the macrophage scavenger receptor, Magn. Reson. Med. 56 (2006) 601–610.
[37] M. Nahrendorf et al., Noninvasive vascular cell adhesion molecule-1 imaging identifies inflammatory activation of cells in atherosclerosis, Circulation 114 (2006) 1504–1511.